Research Article

Analysis on Flow Induced Motion of Cylinders with Different Cross Sections and the Potential Capacity of Energy Transference from the Flow

Jijian Lian, Xiang Yan, Fang Liu, and Jun Zhang

State Key Laboratory of Hydraulic Engineering Simulation and Safety, Tianjin University, No. 92, Weijin Road, Nankai District, Tianjin 300072, China

Correspondence should be addressed to Fang Liu; fangliu@tju.edu.cn

The energy in flow induced motion (FIM) was harnessed in recent years. In this study, the energy transfer ratio was derived to estimate the energy transference from the flow to the FIM. Then the FIM characteristics and energy transference of cylinders with different cross sections were experimentally investigated. The main findings are listed as follows. (a) Circular cylinders and diamond prisms both present a self-limited motion. The maximum amplitude ratio of circular cylinder is around 1~1.2 which is higher than that of diamond prism (0.4~0.5). (b) Triangle prisms and right square prisms present a self-unlimited motion. For triangle prism, amplitude ratio increases over 1.8; for right square prisms, amplitude ratio reaches 1.2. (c) The maximum transfer ratios of circular cylinder and triangle prism are 80% and 57%, respectively, which are much higher than those of other prisms, indicating that circular cylinder and triangle prism have better performances in energy transference. (d) The transfer ratio is strongly dependent on the damping and mass; higher damping or mass will promote a higher transfer ratio. (e) Beyond the critical transfer ratios, amplitude variation coefficients are around 10%~30% resulting in a better performance in stationarity.

1. Introduction

Flow induced vibration (FIV) is a common phenomenon which can be observed in many engineering fields. Many structures such as long-spanned bridges [1], marine risers [2], wind turbine towers, and power-transmission cables have been damaged mainly because of FIM. Vortex-Induced Vibration (VIV), as one of the most common FIV phenomena, was firstly observed by Leonardo da Vinci in a simple way, in circa 1500 AD. When the incoming flow was at an appropriate velocity, vortices alternately shed from either side of the bluff body leading the different distribution of pressure on the surface of the body which resulted in the transverse motion [3]. In the past fifty years, many scholars have devoted themselves to the studies of VIV. Feng [4] firstly used experimental method to investigate the oscillating displacement, the vortex shedding frequency, and the phase angle in a wind tunnel by using 3-inch diameter circular and D-section cylinders. Similar experiments were then performed in a

water tunnel by Bearman [5], and a mathematical model was established to predict the VIV performance of the circular cylinder. Sarpkaya [6] and Williamson and Govardhan [7] used reduced velocities $U_r = U/(f_n \cdot D)$ to predict the synchronization or lock-in region and used the evolution of wake mode to explain the self-limited feature in VIV, where f_n is the natural frequency, and D is the diameter of the cylinder. Their further studies [8–10] reported that the VIV performance was strongly dependent on the combined parameter $m^*\zeta$, where m^* is the mass ratio (the ratio of oscillating mass to displaced fluid mass, $m^* = m_{\text{osc}}/m_d$) and ζ is the system damping ratio. At low $m^*\zeta$ (the cylinder is usually immersed in water) four branches were observed in the amplitude response. They were the initial branch, upper branch, lower branch, and desynchronization branch. Recently, Raghavan and Bernitsas [11] reported that the Reynolds number had great impacts on the peak of amplitude, the lower branch, and the desynchronization branch for circular cylinders with larger diameters. Except for the

circular cylinder, other cylinders or prisms with symmetric cross sections can also produce VIV. Nemes and Zhao and et al. [12, 13] reported that the incident angle had a significant influence on the performance of square cylinders. When the incident angle was 45 degrees (diamond cross section), the cylinder presented a self-limited motion.

Galloping, as another common FIV phenomenon, is defined as a motion with large amplitude and low frequency [14]. The transverse galloping usually occurs in the motion of cylinders with sharp sections such as triangle prisms or rectangular prisms immersed in steady flow due to the periodic variation of attack angle [15]. Den Hartog [14] first used the quasi-steady hypothesis to predict the performance of galloping and fluid forces. Parkinson [16] reported that once galloping started some nonlinear features such as the hysteretic behavior were observed. Contrary to VIV, galloping is not a self-limited motion. As the velocity increases, the amplitude monotonically increases until the bluff body reaches the limitation and is damaged. Because of the huge destruction from the galloping to the structures, which is much larger than that of VIV, many researchers [17–20] focused on the studies of stability and influential factors to predict and control galloping in the past few decades.

Contrary to suppressing the FIM, utilizing the energy from the FIM was a new idea in recent years. To power electronic components, the piezoelectric transducer using aeroelastic oscillation energy was invented for replacing small batteries [21, 22]. Mehmood et al. [23] suggested that the load resistance had a significant effect on the oscillation amplitude, lift coefficient, voltage output, and harvested power in the piezoelectric transducer. In addition to the piezoelectric transducer, another interesting hydrokinetic energy convertor named VIVACE (Vortex-Induced Vibration for Aquatic Clean Energy) convertor was developed by Bernitsas et al. [24, 25] and coworkers based on a similar concept. This convertor, which contains advantages of high energy density, low operable flow velocities, and low maintenance cost, harnessed the hydroelastic oscillation power of the circular cylinder in FIM with PTC [26] immersed in steady fluid flow. In order to accurately investigate the influences of damping, mass, and stiffness, a virtual damper-spring system (V_{ck}) was built by Lee et al. [27] and further improved by Sun et al. [28]. The measured results showed an excellent agreement between the V_{ck} and the real springs and dampers.

The majority of researchers used theoretical [29–31] or numerical methods [23, 32, 33] to investigate the FIM characteristics and the energy extracting. Meanwhile, most FIM experiments were performed in wind tunnels [17–20, 34], and large numbers of them only focus on a cylinder with a certain cross section [23–26, 35–37]. Only limited studies used experimental methods to study the FIM characteristics and the mechanical energy of cylinders with different cross sections. In fact, FIM usually occurs in a combined mode of VIV and galloping. At certain velocities, VIV may occur; at some velocities, galloping may occur; at other velocities, the transmission of VIV and galloping may occur.

This study focuses on the characteristics of FIM and the potential capacity of energy transfer from the incoming flow for cylinders with different cross sections using experimental
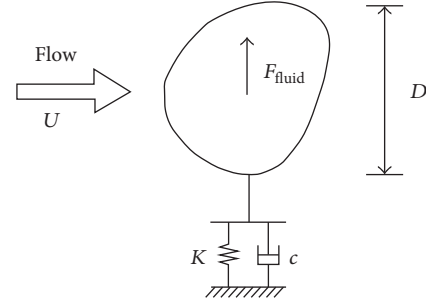

Figure 1: Sketch of flow induced motion of the cylinder in the transverse direction.

methods. In Section 2, the energy transfer ratio is derived based on the motion of the single-degree freedom system, and the influential factors are analyzed. In Section 3, the experimental setup, the physical models, the measurements, and the verifications are described. In Section 4, the characteristics of FIM for different cylinders are compared and analyzed. In Section 5, the energy transfer ratio and the capacity of energy transference are discussed. The effects of the influential factors on the transfer ratio are analyzed. In Section 6, the deviation ratio of oscillating amplitude is introduced to estimate the stationarity of oscillation. Then the relationship between the energy transfer ratio and the stationarity is discussed. The conclusions are summarized at the end.

2. Mathematical Model

2.1. The Motion of a Cylinder. A simplified configuration of a spring-mounted cylinder, with any cross section sharp prone to FIM under the action of an incoming flow in the transverse direction, is considered, as shown in Figure 1. The motion of the cylinder in the y-direction is modeled by a second-order linear equation as follows:

$$m_{\text{osc}}\ddot{y} + c\dot{y} + Ky = F_{\text{fluid}}\hat{y}, \tag{1}$$

where m_{osc} is the oscillating mass of the system, which is the sum of cylinder mass m_{cyl}, transmission mass m_{tra}, and one-third of the spring mass m_{spr}; c is the mechanical damping coefficient; K is the stiffness of the oscillating system; $\ddot{y}$, $\dot{y}$, and y are the acceleration, the velocity, and the displacement of the oscillator, respectively; $\hat{y}$ is the unit normal vector in the transverse direction; and F_{fluid} is the force exerted by the fluid on the body in the transverse direction. Generally, F_{fluid} can be decomposed into viscous and inviscid components as follows:

$$F_{\text{inviscid}}\hat{y} = -m_a\ddot{y}, \tag{2a}$$

$$F_{\text{viscous}}\hat{y} = \frac{1}{2}c_y\rho U^2 DL, \tag{2b}$$

where m_a is the added mass (for circular cylinder, m_a is approximately equal to 1); c_y is the instantaneous lift force coefficient; ρ is the water density; U is the free-stream flow
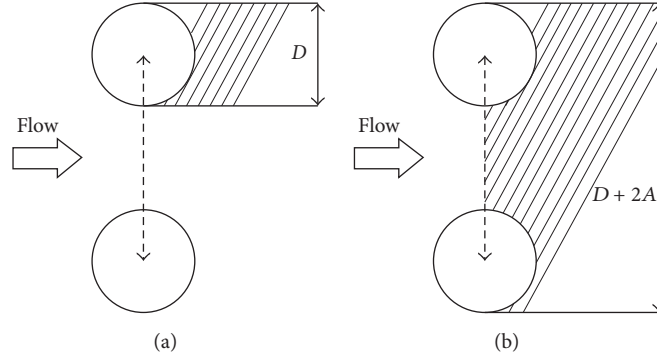
Figure 2: The projected area for the calculation of power in fluid P_w. (a) The projected area of cylinder; (b) the projected area of the vibration.

velocity; D is the characteristic dimension of the body normal to the flow (for circular cylinder, D is the diameter of the cylinder); and L is the length of cylinder. Then the equation of motion could be derived as

$$(m_{osc} + m_a)\,\ddot{y} + c\dot{y} + Ky = \frac{1}{2}c_y\rho U^2 DL. \tag{3}$$

Bearman [5] reported that FIM could be regarded as a sinusoidal motion, and the lift force acted on the bluff bodies can also be regarded as a sinusoidal force. Then the transverse displacement and the lift force coefficient can be obtained as the functions of the time t.

$$y = A \cdot \sin\left(2\pi f_{osc}t\right), \tag{4a}$$

$$c_y = C_y \sin\left(2\pi f_{fluid}t + \phi\right), \tag{4b}$$

where A is the amplitude of the oscillation displacement; f_{osc} is the dominant frequency of oscillation; C_y is the maximum lift force coefficient; f_{fluid} is the dominant frequency of lift force; and ϕ is the difference of phase angle between the lift force and the displacement. For stable oscillation, f_{fluid} is approximately equal to f_{osc}, $f_{fluid} = f_{osc}$.

2.2. The Mechanical Power of Oscillator. In order to harness the energy in FIM, the flow energy must be transformed through two steps. Firstly, the kinetic energy in the incoming flow should be transferred to the oscillating mechanical energy. Then only a part of mechanical energy is extracted by the convertor, and the rest is dissipated due to the mechanical damping of the transmission part and the convertor. The mechanical energy is the base of the harnessed energy, and the transfer ratio, which is the ratio of the mechanical energy to the flow energy, will affect the conversion ratio directly. Consequently, the expression of mechanical energy in FIM is derived in this section.

The mechanical energy of the oscillator can be obtained by integrating the left hand side of (3) after multiplying the instantaneous velocity. Then the mean mechanical power P_{Mech} in a period T_{osc} can be written as

$$P_{Mech} = \frac{1}{T_{osc}}\int_0^{T_{osc}} \left[(m_{osc} + m_a)\,\ddot{y} + c\dot{y} + Ky\right] \cdot \dot{y}\,dt. \tag{5}$$

The displacement y of FIM is assumed as a sinusoidal function of time t (see (4a)). Then P_{Mech} can be simplified as

$$P_{Mech} = \frac{1}{T_{osc}}\int_0^{T_{osc}} c \cdot \left(\dot{y}\right)^2 dt. \tag{6}$$

Then P_{Mech} can be further derived as

$$P_{Mech} = 2\pi^2 c f_{osc}^2 A^2. \tag{7}$$

Equation (7) shows that the damping coefficient of the oscillating system c, the dominant frequency of oscillation f_{osc}, and the amplitude of the displacement A have great impacts on the mechanical power.

2.3. The Energy Transfer Ratio. The mechanical energy of oscillating cylinders originally comes from the kinetic energy in flow. Until now, previous studies have different opinions on calculating the flow energy P_w. Some researchers believe that P_w is the kinetic energy of the flow over the projected area of the cylinder DL (as seen in Figure 2(a)). Others believe that P_w is the kinetic energy of the flow over the projected area of the cylinder and the oscillation $(D + 2A)L$ (as seen in Figure 2(b)). The expressions are presented, respectively, as follows:

$$P_w = \frac{1}{2}\rho U^3 DL, \tag{8a}$$

$$\text{Or } P_w = \frac{1}{2}\rho U^3 \left(D + 2A\right) L. \tag{8b}$$

Then the transfer ratio can be derived according to (7), (8a), and (8b). Here, we use the symbol "η" to represent the transfer ratio. Then the expressions can be written as

$$\eta = \frac{P_{Mech}}{P_w} = \frac{2\pi^2 c f_{osc}^2 A^2}{(1/2)\,\rho U^3 DL}, \tag{9a}$$

$$\text{Or } \eta = \frac{P_{Mech}}{P_w} = \frac{2\pi^2 c f_{osc}^2 A^2}{(1/2)\,\rho U^3 \left(2A + D\right) L}. \tag{9b}$$

Based on the transfer ratio, the capacity of energy transference from the flow can be efficiently estimated.
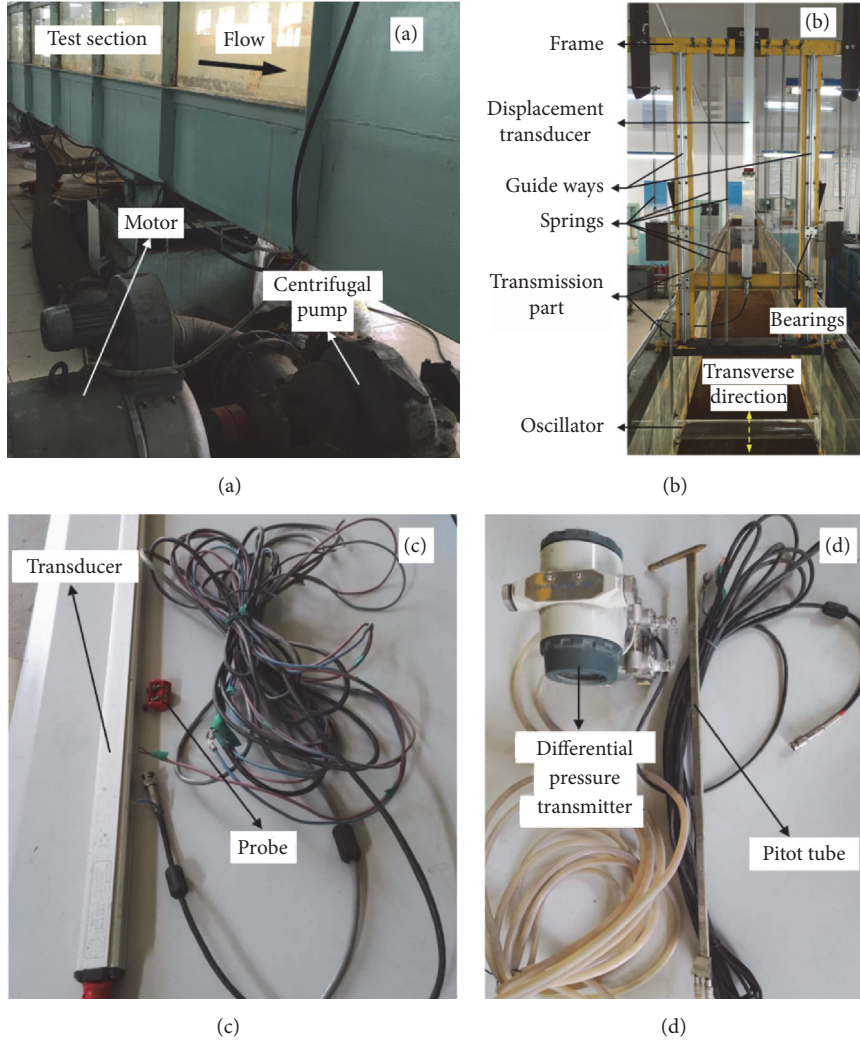
FIGURE 3: The experimental setup and the physical model. (a) Circular water channel; (b) experimental setup; (c) displacement transducer; (d) Pitot tube and differential pressure transmitter.
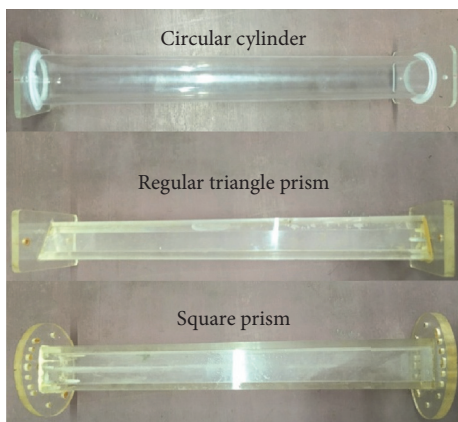

FIGURE 4: The physical models of cylinders or prisms.

Then the damping ratio ζ and the natural frequency f_n of the oscillating system are introduced as follows:

$$\zeta = \frac{c}{2\sqrt{m_{\text{osc}}K}}, \tag{10}$$

$$f_n = \frac{1}{2\pi}\sqrt{\frac{K}{m_{\text{osc}}}}. \tag{11}$$

The energy transfer ratio can be further derived as

$$\eta = \frac{8\pi^3 \zeta m_{\text{osc}} f_n f_{\text{osc}}^2 A^2}{(1/2)\,\rho U^3 DL}, \tag{12a}$$

$$\text{Or } \eta = \frac{8\pi^3 \zeta m_{\text{osc}} f_n f_{\text{osc}}^2 A^2}{(1/2)\,\rho U^3 (2A+D)\,L}. \tag{12b}$$

Then the displaced fluid masses m_d for cylinders or prisms with different cross sections are introduced as
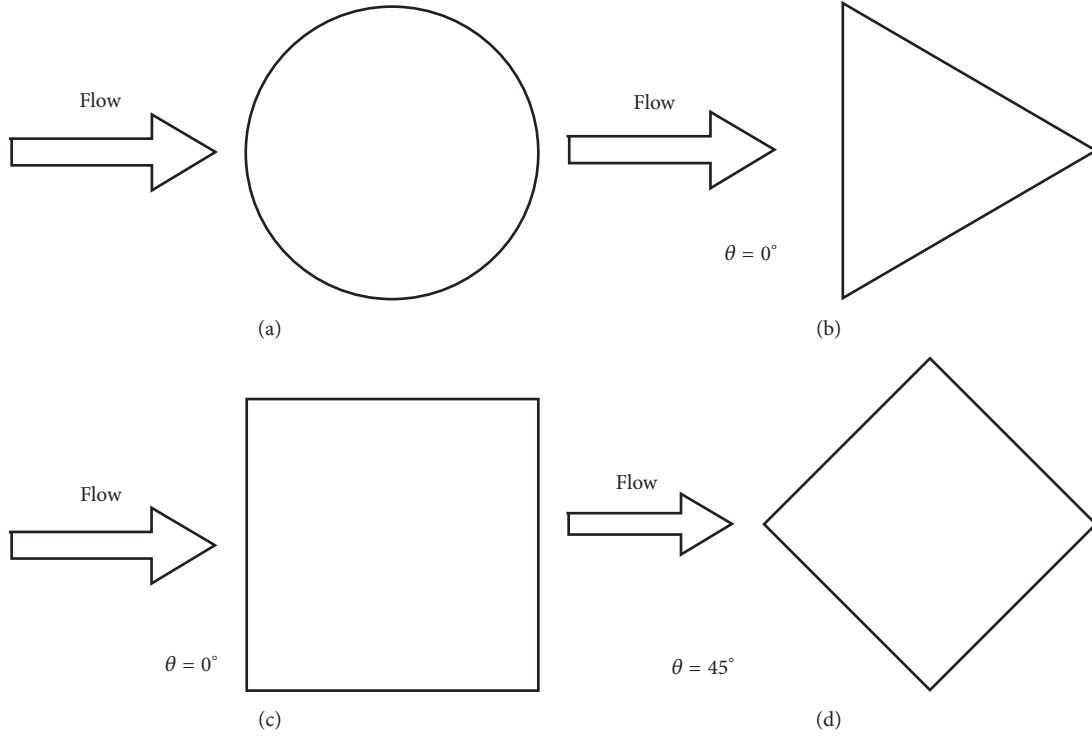
$$m_d = \alpha \rho D^2 L, \tag{13}$$

FIGURE 5: The incident angle to the flow direction for different cylinders. (a) Circular cylinder; (b) regular triangle prism; (c) right square prism; (d) diamond square prism.
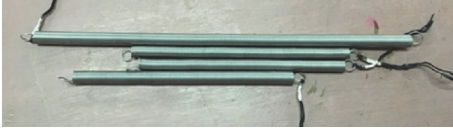

FIGURE 6: The different extension springs used in the experiments.

where α represent different cross sections. For the circular cylinder, α is $\pi/2$; for the regular triangle prism, α is $\sqrt{3}/4$; for right square or diamond prism, α is 1.

Then the transfer ratio could be nondimensionalized as follows:

$$\eta = \frac{16\pi^3 \alpha m^* \zeta f^{*2} A^{*2}}{U_r^3}, \tag{14a}$$

$$\eta = \frac{16\pi^3 \alpha m^* \zeta f^{*2} A^{*2}}{U_r^3 (2A^* + 1)}, \tag{14b}$$

where A^* is the amplitude ratio, $A^* = A/D$; f^* is the frequency ratio, $f^* = f_{\rm osc}/f_n$; and U_r is the reduced velocity of flow, $U_r = U/(D \cdot f_n)$.

As we all know, the performances of the amplitude and the frequency are strongly dependent on the cross section, the mass, the damping, and the velocity. Therefore, the performances of transfer ratio η are subsequently dependent on the cross section, the mass, the damping, and the velocity according to (14a) and (14b).

Based on the factors above, an experimental setup was established and verified in Section 3. Then the characteristics of FIM and the energy transfer ratio were analyzed in Sections 4 and 5.

3. Experimental Method

3.1. Facility and Apparatus. A continuous flow past a cylinder is provided in the circulating water channel in the TJU Hydraulics Laboratory (Figure 3(a)). The channel is 15 m long, 0.6 m wide, and approximately 0.45 m deep. A centrifugal pump with a 45 kW motor is used to drive the water in the channel. A gearbox is used to control the flow speed. The range of flow speed is from 0.20 m/s to 0.75 m/s. The physical model of the oscillation system is installed in the middle of the channel.

The physical model consists of the frame, the guide ways, the transmission part, the oscillators, and the springs. The frame is made of iron located on the top of the channel. Two linear guide ways are fixed on the frame in the vertical direction to the incoming flow. The transmission part is forced to move on the guide ways in the transverse direction by using four linear bearings. Both end sides of the oscillator are fixed on the foot of the transmission section. The top and bottom of the springs are fixed on the transmission section and the frame, respectively. Then the oscillators can have an alternately linear motion in the transverse direction to the incoming flow. A magnetic induction displacement transducer is fixed on the middle of the frame in the transverse
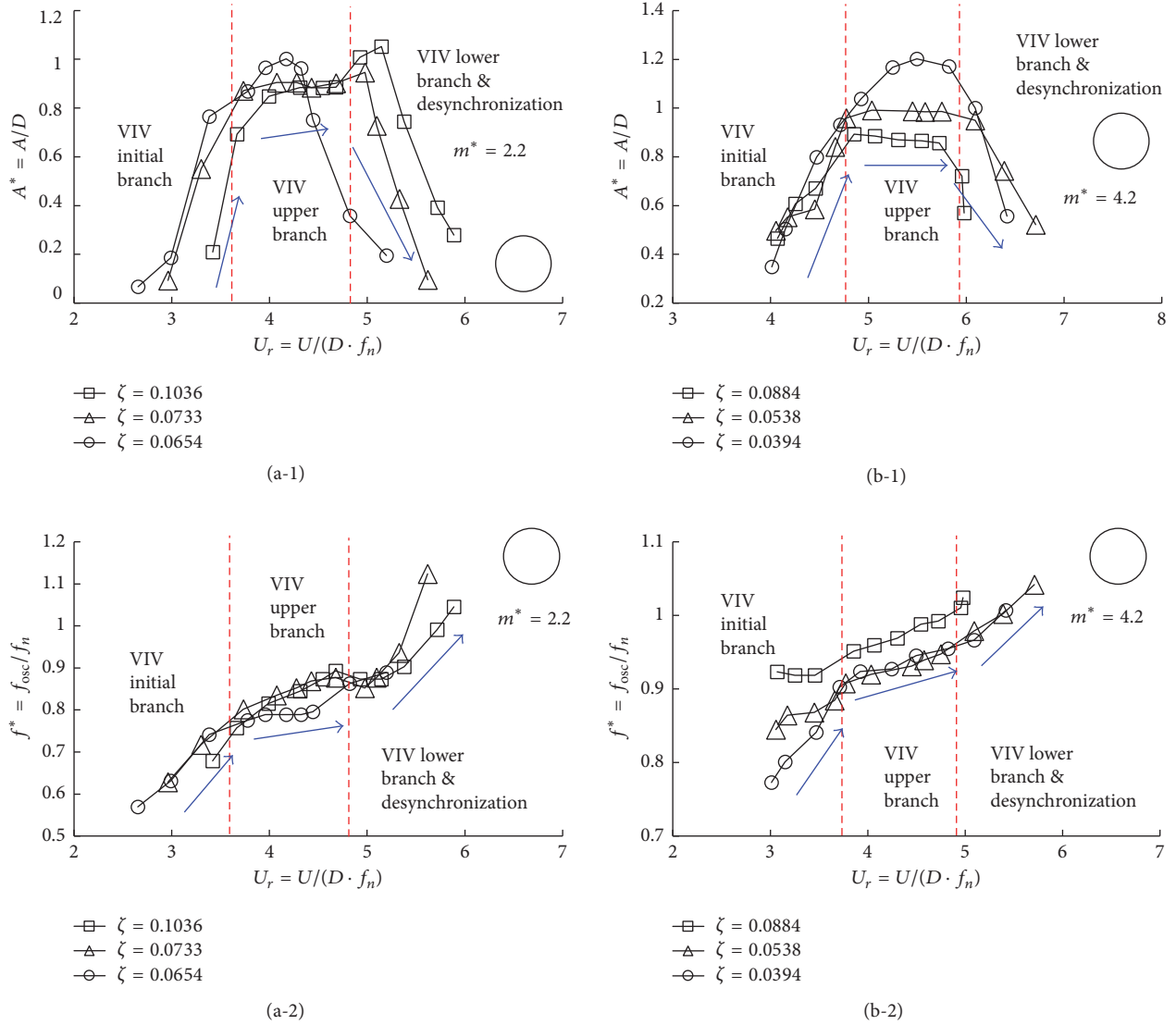
FIGURE 7: Variations of the amplitude ratios and the frequency ratios against the reduced velocities for circular cylinders. Amplitude ratio $A^* = A/D$; frequency ratio $f^* = f_{osc}/f_n$; reduced velocity $U_r = U/(f_n D)$; damping ratios $\zeta = c/2\sqrt{m_{osc}K}$; mass ratios $m^* = m_{osc}/m_d$; f_n is the natural frequency. (a-1) The responses of amplitude ratios, $m^* = 2.2$; (a-2) the responses of frequency ratios, $m^* = 2.2$; (b-1) the responses of amplitude ratios, $m^* = 4.2$; (b-2) the responses of frequency ratios, $m^* = 4.2$.

TABLE 1: The physical parameters of different oscillators.

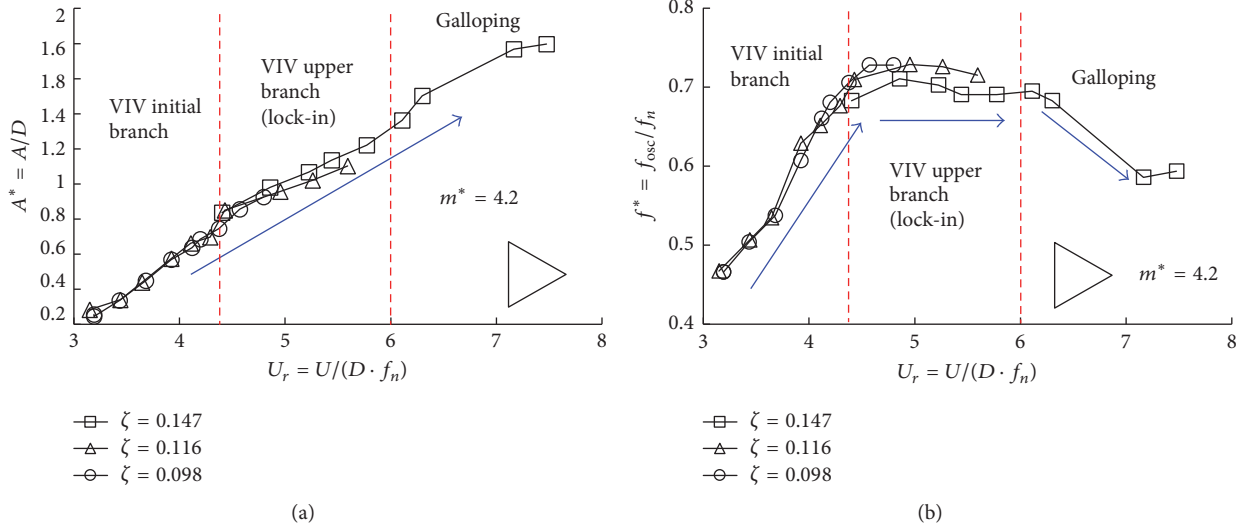| Cross section	Circular	Regular triangle	Right square	Diamond square
Cross section factor α	$\pi/2$	$\sqrt{3}/4$	1	1
Displacement mass m_d/kg	1.414	0.779	1.800	1.800
m_{cyl}/kg	0.579	0.724	1.407	1.407
m_{tra}/kg	2.553	2.553	2.553	2.553
$m^* = 2.2$				
$\quad m_{add}$/kg	0.000	—	0.000	0.000
$\quad m_{osc}$/kg	3.132	—	3.960	3.960
$m^* = 4.2$				
$\quad m_{add}$/kg	2.825	0.000	3.622	3.622
$\quad m_{osc}$/kg	5.957	3.277	7.582	7.582

(a)

(b)

FIGURE 8: Variations of the amplitude ratios and the frequency ratios against the reduced velocities for regular triangle prism. Amplitude ratio $A^* = A/D$; frequency ratio $f^* = f_{osc}/f_n$; reduced velocity $U_r = U/(f_n D)$; damping ratios $\zeta = c/2\sqrt{m_{osc} K}$; mass ratios $m^* = m_{osc}/m_d$; f_n is the natural frequency. (a) The responses of amplitude ratios, $m^* = 4.2$; (b) the responses of frequency ratios, $m^* = 4.2$.

TABLE 2: The different stiffness groups.

Number	System stiffness/N·m^{-1}
1	99
2	199
3	301
4	400
5	505
6	602

direction to measure the oscillating displacement as shown in Figure 3. The measurement range is from 0 to 800 mm. The accuracy of the displacement transducer is within ±0.05%, giving a displacement measurement resolution of 0.001% FS. The rod is fixed on the top of the transmission section. The flow velocity measurement is performed using the Pitot tube with a differential pressure transmitter, which is positioned about 1 m in front of the prism. The accuracy of the differential pressure transmitter is within ±0.1% of the 6 kPa linear range available, and its resolution is within 0.1% FS. All data are collected at a 50 Hz sampling rate. Other details had been introduced by Zhang et al. [38].

3.2. Oscillators. Four typical cylinders and prisms with different cross sections are selected in the present experiments. They are circular cylinders, regular triangle prisms, and right square prisms, as shown in Figure 4. The characteristic dimensions D of the oscillators are 0.06 m; the lengths L of the oscillators are approximately 0.5 m. The oscillators are composed of Plexiglas. Two end plates are fixed on the two end sides of the oscillators, respectively (Figure 4), and the gaps between the end plates and the walls of the channel are less than around 1 cm. Then the boundary effects can be reduced significantly [39–41].

For circular cylinders, different incident angles hardly affect the performance of the motion due to the axisymmetric cross section. But for other prisms the different incident angles strongly affect the performances. Some studies reported that the triangle prisms can achieve fully developed transverse galloping with high amplitude and stable frequency when the base of the triangle is vertical to the coming flow (the incident angle is zero). But in other configurations (the incident angle is not zero) the triangle prisms cannot achieve it. Thus, only one configuration of triangle prism, in which the base is vertical to the coming flow, is selected in present experiments (as seen in Figure 5(b)). In addition to the triangle prisms, the performances of the square prisms are more complicated while the incident angles are changing [12, 13]. Two typical configurations for square prism are selected in present experiment. They are right square prisms (the incident angle is zero) and diamond prisms (the incident angle is 45 degree) shown in Figures 5(c) and 5(d).

3.3. Mass and Stiffness. Inside the oscillators, there is room to insert additional weight m_{add} to change the oscillating mass m_{osc} to control the mass ratio m^* of oscillators. For the circular cylinders, the right square prisms, and the diamond prisms, two mass ratios are selected, 2.2 and 4.2. For the regular triangle prisms, the mass ratio of regular triangle prism cannot be decreased to 2.2 due to the limitations of the experimental setup. Only the configuration with $m^* = 4.2$ is selected for the regular triangle prism in present experiment. The details of mass of each oscillator are illustrated in Table 1.

A linear stiffness system is needed to investigate free oscillation. In the present study, the linear stiffness system is composed of different physical extension springs, shown in Figure 6. Then different system stiffness can be modeled by using different groups of springs. The stiffness of a spring

(a-1)   (b-1)

(a-2)   (b-2)
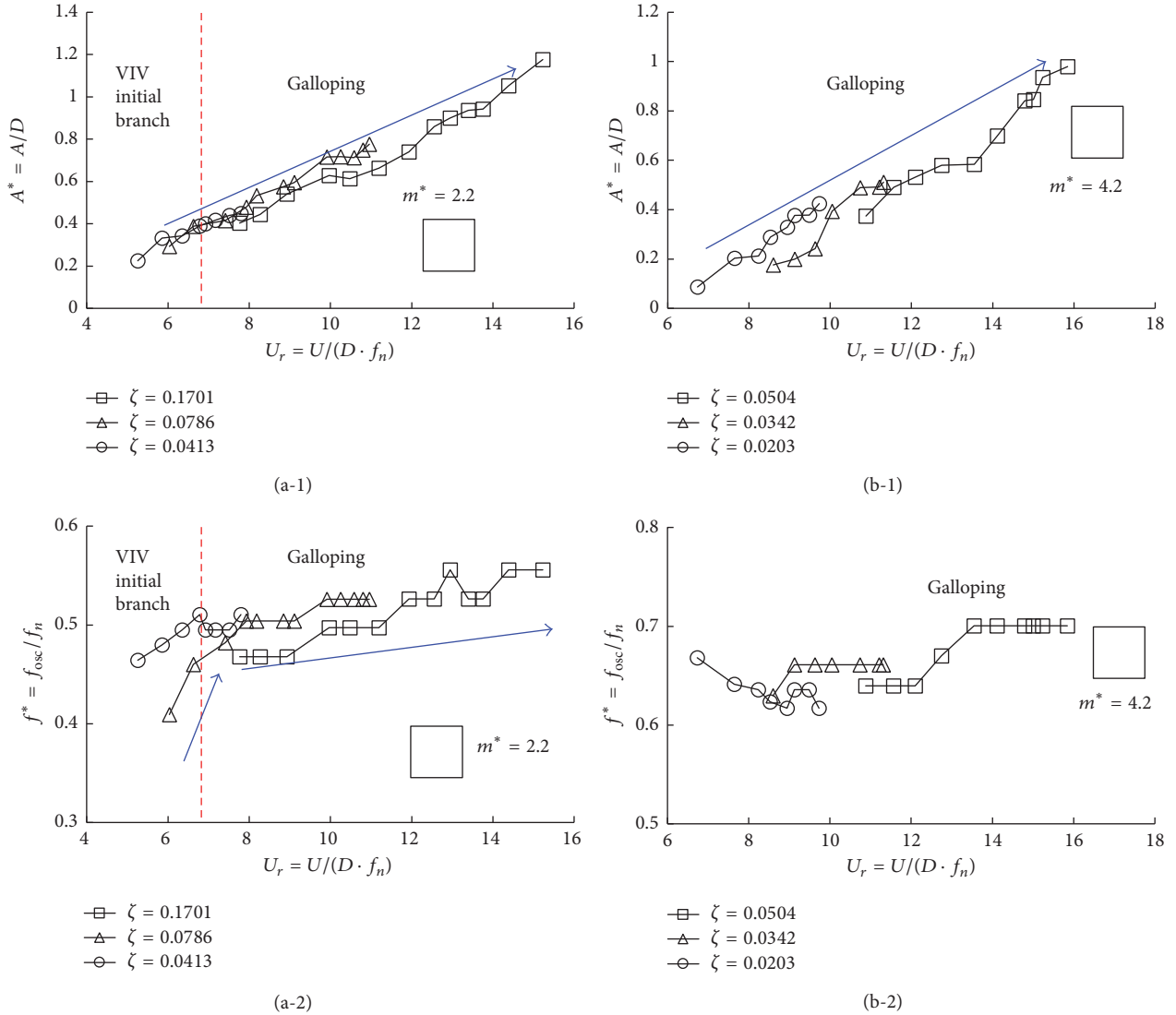
FIGURE 9: Variations of the amplitude ratios and the frequency ratios against the reduced velocities for right square prism. Amplitude ratio $A^* = A/D$; frequency ratio $f^* = f_{osc}/f_n$; reduced velocity $U_r = U/(f_n D)$; damping ratios $\zeta = c/2\sqrt{m_{osc}K}$; mass ratios $m^* = m_{osc}/m_d$; f_n is the natural frequency. (a-1) The responses of amplitude ratios, $m^* = 2.2$; (a-2) the responses of frequency ratios, $m^* = 2.2$; (b-1) the responses of amplitude ratios, $m^* = 4.2$; (b-2) the responses of frequency ratios, $m^* = 4.2$.

group with n springs is the sum of each spring stiffness $k_{spr,i}$ in the group.

$$K = \sum_{i=1}^{n} k_{spr,i}. \qquad (15)$$

Six spring groups are selected in our experiment. The range of stiffness is varied from around 100 N/m to 600 N/m. The details are presented in Table 2.

3.4. Free Decay Tests and Validation. The damping ratio ζ is another key factor affecting the transfer ratio. In this section, the values of the damping ratios in different configurations were obtained by performing free decay tests. In order to guarantee the accuracy of results, every configuration was

repeated four times in this experiment. The final results were determined using a simple average method.

Depending on the test results, the damping ζ could be calculated using the logarithmic decrement method, which is expressed as

$$\zeta = \frac{\ln \eta}{2\pi} = \frac{1}{2\pi} \ln\left(\frac{A_i}{A_{i+1}}\right), \qquad (16)$$

where A_i denotes the amplitudes in the ith peak, which were measured in the free decay tests.

Meanwhile, the natural frequencies of the system in different configurations were extracted using FFT from the time histories of the displacements measured in the free decay tests. The natural frequencies were then calculated by theoretical method and compared with the measured results
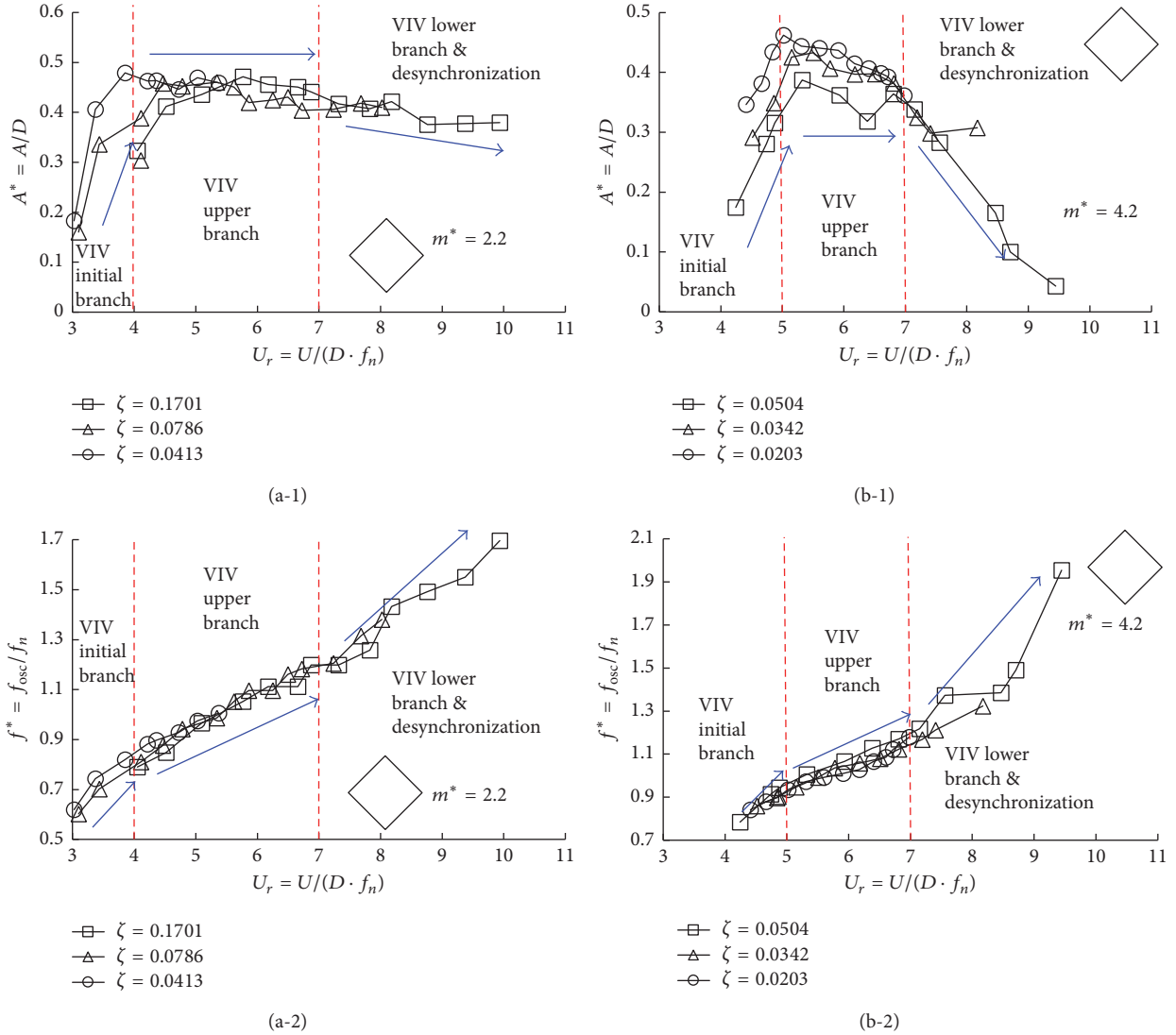
Figure 10: Variations of the amplitude ratios and the frequency ratios against the reduced velocities for diamond prism. Amplitude ratio $A^* = A/D$; frequency ratio $f^* = f_{osc}/f_n$; reduced velocity $U_r = U/(f_n D)$; damping ratios $\zeta = c/2\sqrt{m_{osc}K}$; mass ratios $m^* = m_{osc}/m_d$; f_n is the natural frequency. (a-1) The responses of amplitude ratios, $m^* = 2.2$; (a-2) the responses of frequency ratios, $m^* = 2.2$; (b-1) the responses of amplitude ratios, $m^* = 4.2$; (b-2) the responses of frequency ratios, $m^* = 4.2$.

to further verify the dynamic reliability of the experimental setup.

When a cylinder is immersed in air, its added mass can be negligible due to the low density and viscosity of air. When a cylinder is immersed in water, the added mass effect should be taken into account. Then the calculated natural frequency in air and in water can be expressed as

$$f_n = \frac{1}{2\pi}\sqrt{\frac{K}{m_{osc}}}, \tag{17a}$$

$$f_{n,w} = \frac{1}{2\pi}\sqrt{\frac{K}{m_{osc} + m_a}} = \frac{1}{2\pi}\sqrt{\frac{K}{m_d(m^* + c_a)}}, \tag{17b}$$

where K and m_{osc} were based on the results in Tables 1 and 2, m_a is added mass, and c_a is added mass coefficient.

For circular cylinder, c_a could be regarded as 1 ($c_a \approx 1$). However, for triangle prism and square prism, $f_{n,w}$ and c_a are very complicated. Until now, different researchers had different opinions on the value of c_a for noncircular cylinders. Our group had tried to reveal $f_{n,w}$ and c_a of triangle prism for different system stiffness K [42]. But the results showed that the measured $f_{n,w}$ did not agree with the calculated $f_{n,w}$. It is difficult to analyze the added mass effect. In order to ensure that the experiment results for different cylinders are compared under the same conditions, we selected the natural frequency in air f_n to calculate the reduced velocity ($U_r = U/(f_n D)$) and frequency ratio ($f^* = f_{osc}/f_n$).

The complete results in the free decay tests are listed in Table 3. $f_{n,cal}$ represents the natural frequency calculated using (17a); $f_{n,mea}$ represents the natural frequency measured in each free decay test; and the expression of error is Error =
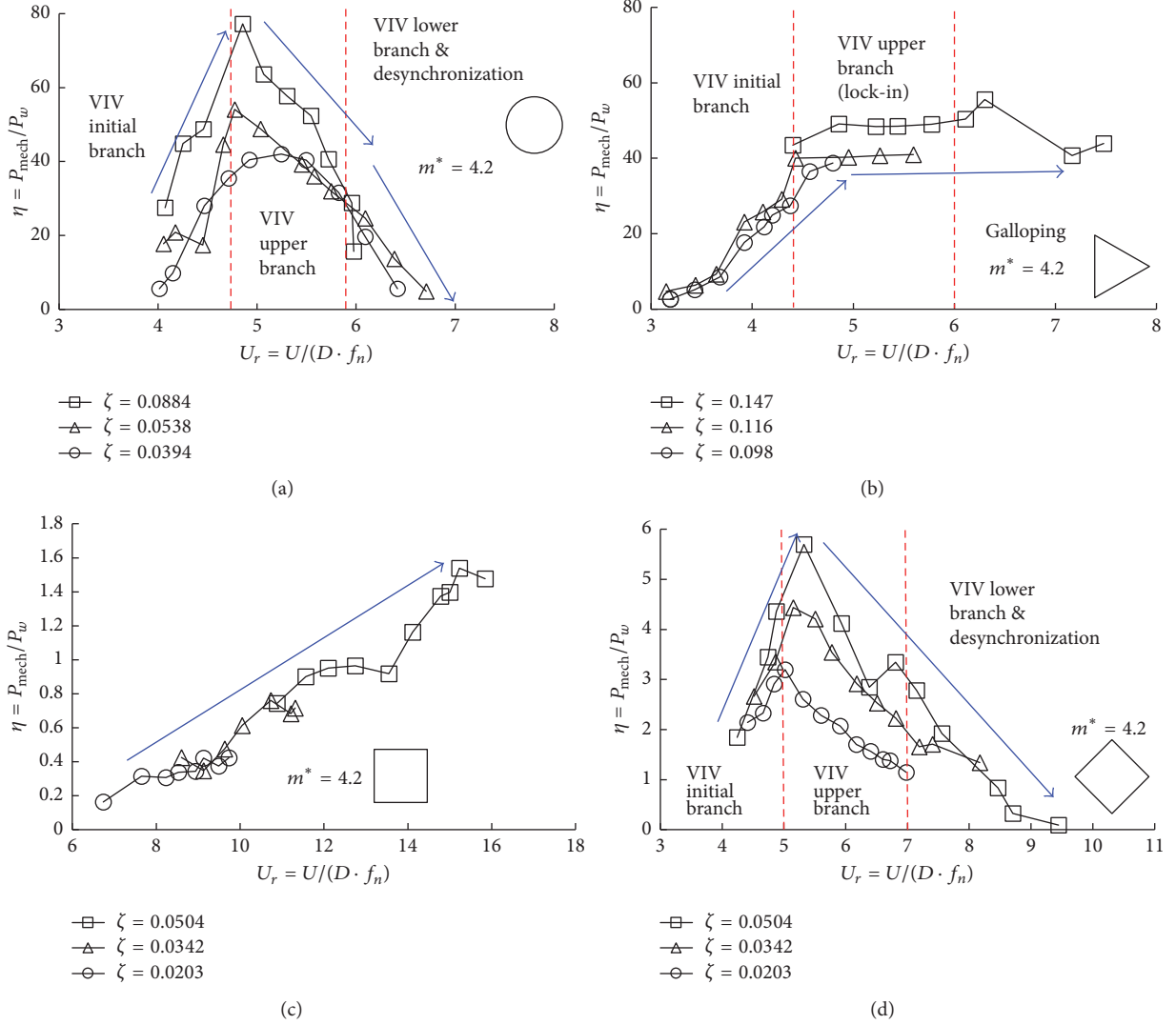
FIGURE 11: Variations of the energy transfer ratios with the reduced velocities for cylinders or prisms with different cross sections. $m^* = 4.2$. (a) Circular cylinders; (b) regular triangle prisms; (c) right square prisms; (d) diamond prisms.

TABLE 3: The complete results in free decay test.

Cross section	m_{osc} (kg)	m^*	K (N/m)	ζ	$f_{n,cal}$ (Hz)	$f_{n,mea}$ (Hz)	Error (f_n) (%)
Circular	3.132	2.2	400	0.1036	1.799	1.748	2.8
Circular	3.132	2.2	505	0.0733	2.020	1.977	2.1
Circular	3.132	2.2	800	0.0654	2.544	2.474	2.8
Circular	5.957	4.2	301	0.0884	1.131	1.098	2.9
Circular	5.957	4.2	400	0.0538	1.304	1.277	2.1
Circular	5.957	4.2	602	0.0394	1.600	1.591	0.6
Square	3.622	2.2	99	0.1701	0.832	0.855	2.8
Square	3.622	2.2	199	0.0786	1.180	1.141	3.3
Square	3.622	2.2	400	0.0413	1.673	1.616	3.4
Square	7.582	4.2	199	0.0504	0.815	0.821	0.6
Square	7.582	4.2	400	0.0343	1.156	1.135	1.8
Square	7.582	4.2	505	0.0203	1.299	1.337	2.9
Triangle	3.227	4.2	199	0.1470	1.250	1.258	0.6
Triangle	3.227	4.2	400	0.1160	1.772	1.755	1.0
Triangle	3.227	4.2	602	0.0980	2.174	2.180	0.3
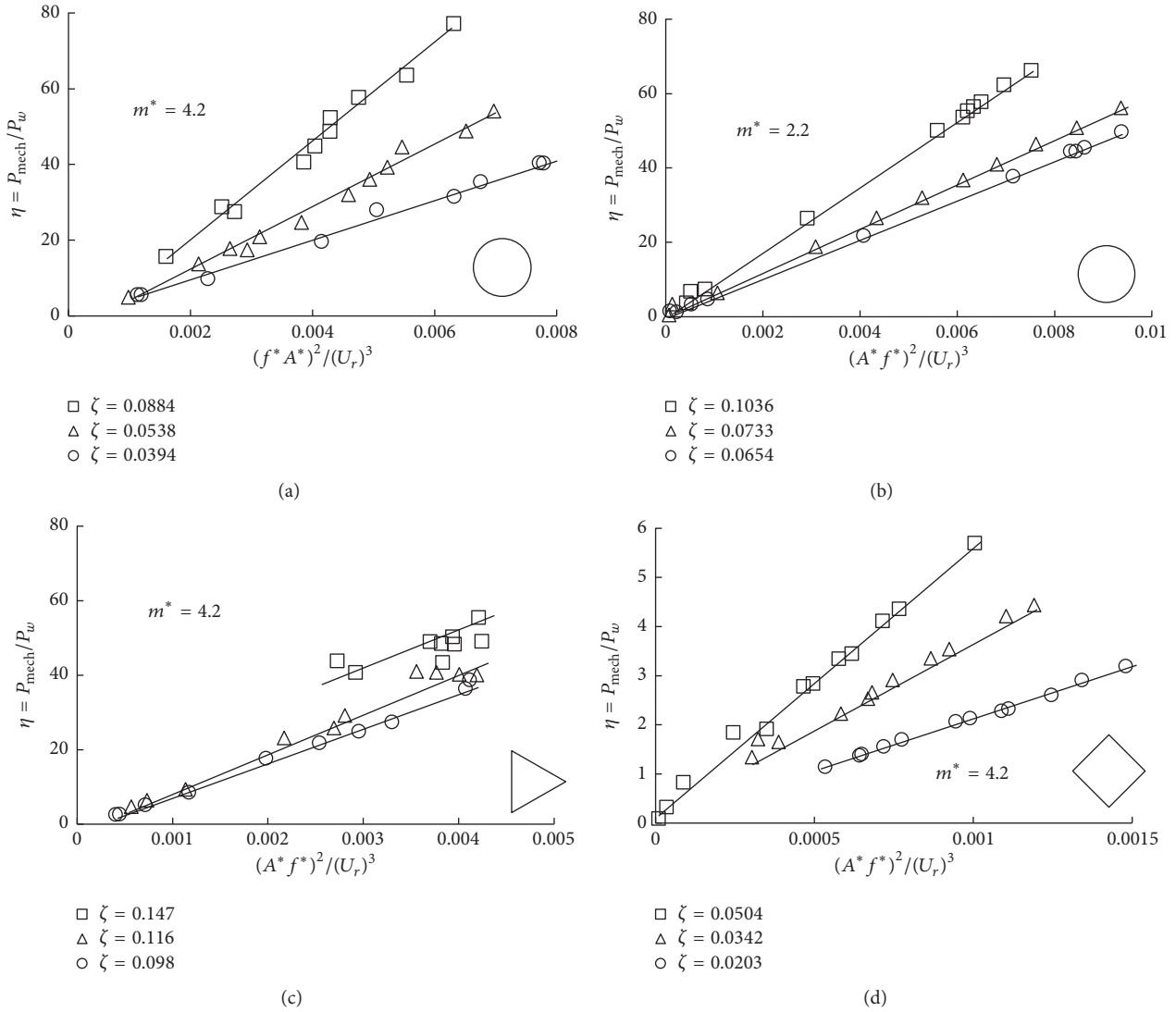
FIGURE 12: Variations of the transfer ratios η against the combined parameters $(A^* f^*)^2 / (U_r)^3$. (a) Circular cylinders, $m^* = 2.2$; (b) circular cylinders, $m^* = 4.2$; (c) regular triangle prisms, $m^* = 4.2$; (d) diamond prisms; $m^* = 4.2$.
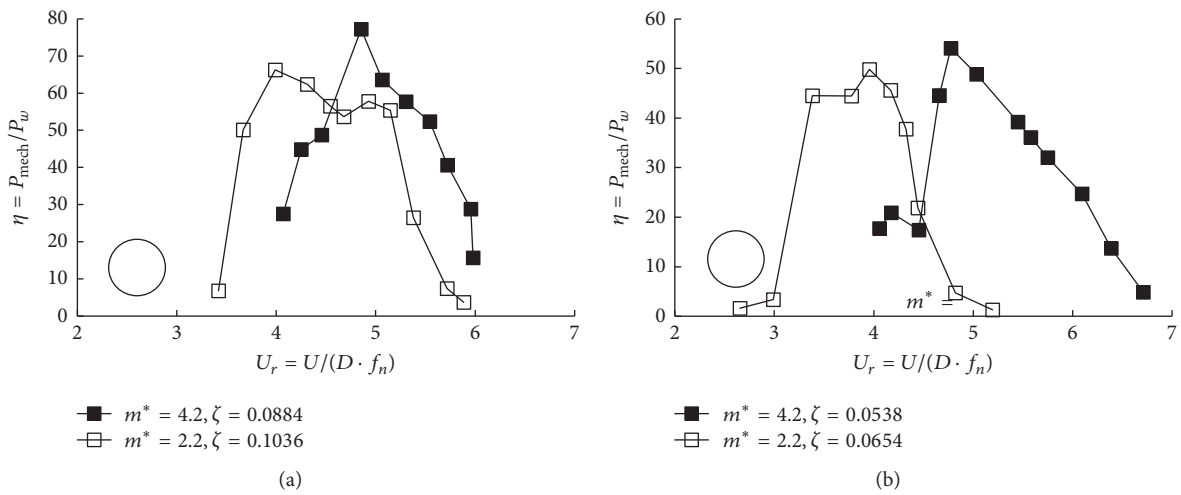
FIGURE 13: The influence of the mass ratio m^* on the transfer ratio η. (a) Case 1. (b) Case 2.
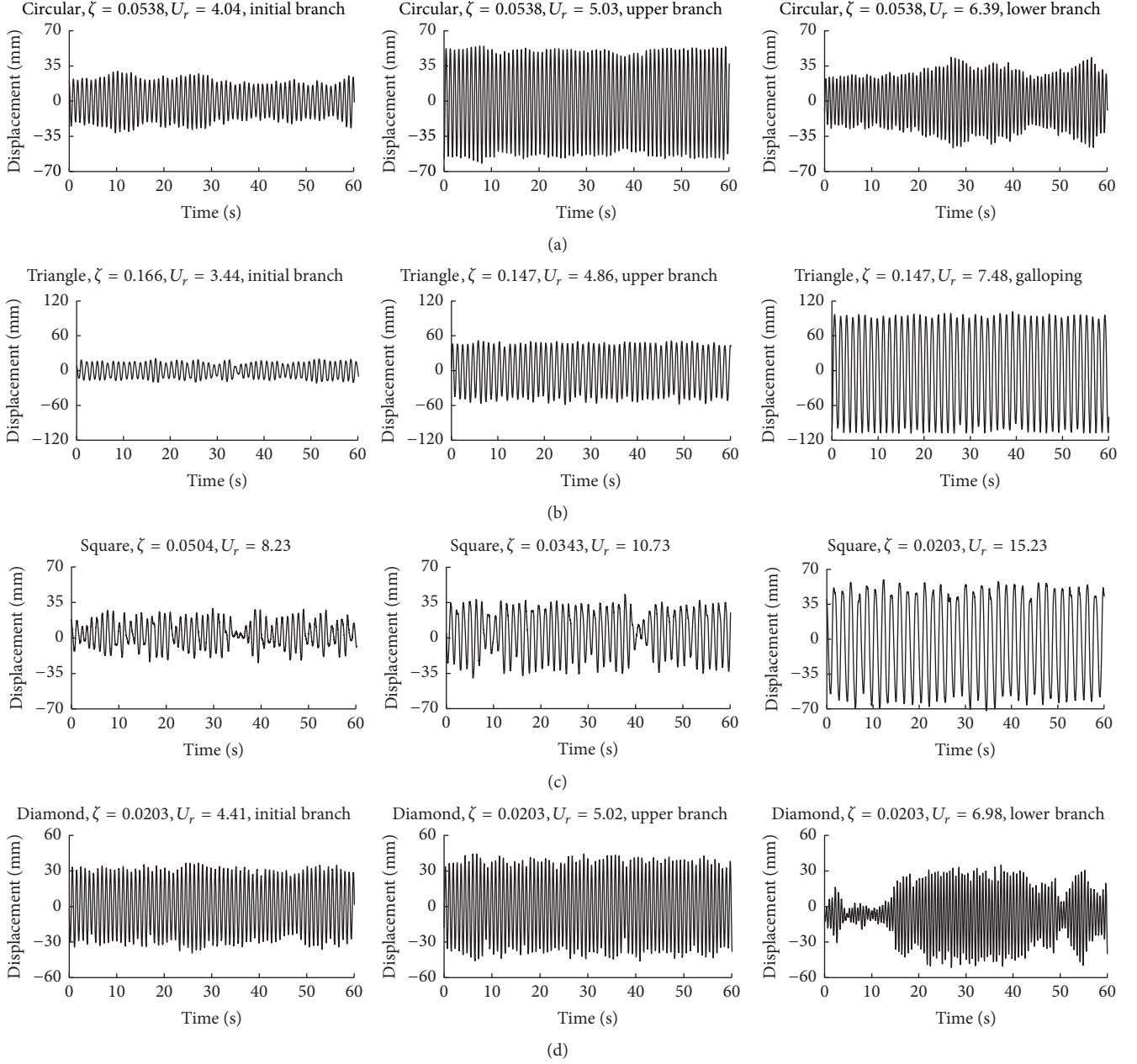
Figure 14: Selected examples of the time histories of displacement in each branch for the cylinders or prisms. (a) Circular cylinders; (b) regular triangle prisms; (c) right square prisms; (d) diamond prisms.

$|f_{n,\mathrm{cal}} - f_{n,\mathrm{mea}}|/f_{n,\mathrm{mea}}$. It is observed that the measured and the calculated natural frequencies have an excellent agreement, and the maximum error is as low as 3.5%, which indicates that the test setup and method are reliable.

The system damping ratio is strongly dependent on the damping coefficient, the oscillating mass, and the system stiffness according to (10). In our experimental setup, there was no positive method or device to change the damping coefficient. The change of damping ratio was mainly dependent on the change of system stiffness. Therefore, the increase of stiffness meant the decrease of the damping ratio.

In the present experiment, we used the established oscillation system, which had been introduced in Zhang et al.'s experiment [38]. The details of validation had also been described in Zhang et al.'s research [38].

4. Experimental Results and Discussion

In this section, the responses of the amplitude and the frequency for circular cylinders, regular triangle prisms, right square prisms, and diamond prisms are discussed, respectively. The variations of A^* and f^* against the reduced velocity U_r for those cylinders or prisms are plotted in Figures
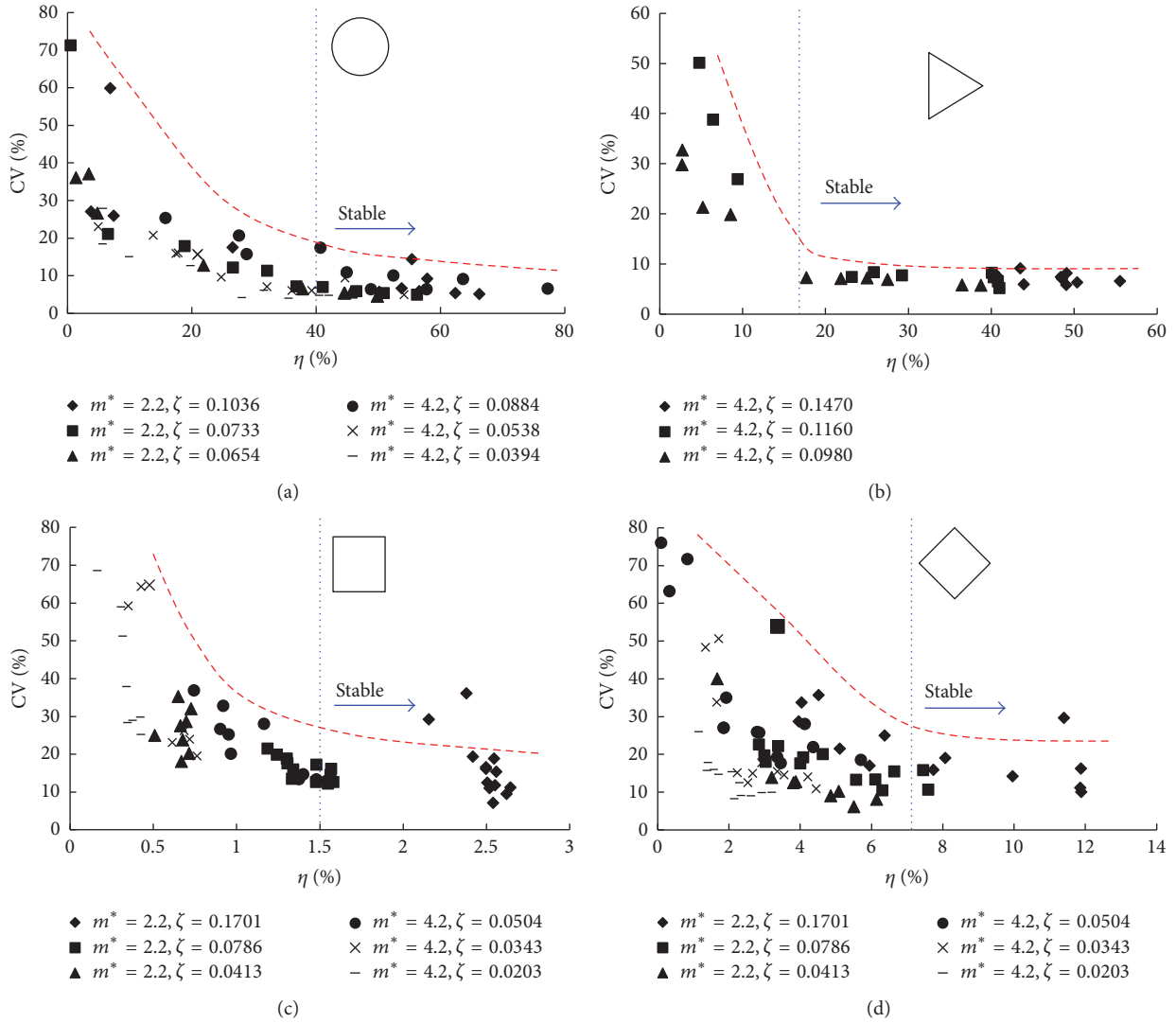
FIGURE 15: Variations of the variation coefficients of amplitude CV with the energy transfer ratios η. (a) Circular cylinders; (b) regular triangle prisms; (c) right square prisms; (d) diamond prisms.

7, 8, 9, and 10. In the figures, A^* is the ratio of amplitude and diameter (A/D), and A is the average of all amplitudes in time histories of displacements measured over 60 seconds. f^* is the ratio of the dominant oscillation frequency and the natural frequency, $f^* = f_{osc}/f_n$, and f_{osc} are also obtained from the time histories of displacements by FFT method. U_r is the reduced velocity, and its expression is $U_r = U/(D \cdot f_n)$. The indexes above are all nondimensional.

4.1. The Response of Circular Cylinder. As the reduced velocity U_r increasing, three branches, which are the initial branch, the upper branch, and the lower branch or the desynchronization, can be observed clearly for all cases (different damping ratios and different mass ratios) in Figure 7. The details of characteristics in each branch for circular cylinder can be summarized as follows.

(a) In the initial branch, the amplitude ratio A^* and the frequency ratio f^* both increase rapidly from small values.

The motion of the circular cylinder initiates at around $U_r = 3\sim4$.

(b) As the reduced velocity U_r increases to the range of upper branch, the amplitude ratio A^* and the frequency ratio f^* both present a jump. Then A^* stays at a high level of approximately 1; f^* increases slowly around 1, too. It indicates that the oscillation is in the lock-in range. The natural frequency and the frequency of lift force are synchronized well.

(c) As the reduced velocity U_r further increases to move away from the range of upper branch (lock-in range), the response of circular cylinder enters the lower branch or desynchronization. In this branch, the frequency ratio f^* increases rapidly again. The frequency of lift force and the natural frequency cannot be synchronized well any more. Therefore, the amplitude ratio A^* collapses rapidly.

(d) Different damping ratios and different mass ratios cause different performances of the oscillation. It is found

that A^* increases with the increase of the damping ratio. In addition, as the mass ratio increases, the ranges of lock-in are also changed. When $m^* = 2.2$, the lock-in range of reduced velocity is about 4 to 5; when $m^* = 4.2$, it is about 5 to 6.

The analysis of the results above reveals that the circular cylinder performs a "self-excited" and "self-limited" VIV in the present experiment. This performance is consistent with the results reported by Khalak and Williamson [8, 9], Govardhan and Williamson [10], and Raghavan and Bernitsas [11].

4.2. The Response of Regular Triangle Prism. Compared with the performance of the circular cylinder (as shown in Figure 7), the lower branch (VIV) is not observed in the response of the regular triangle prism (as shown in Figure 8). Instead, a galloping branch is observed after the reduced velocity exceeds $U_r = 6$. The amplitude ratio A^* of the prism monotonically increases as the reduced velocity U_r increases. Even when U_r is over 7, the trend of amplitude ratio A^* still shows no sign of decrease. This performance is "self-excited" but not "self-limited," which is different from the circular cylinder. Similar results of regular triangle prisms were reported by Alonso and Meseguer [15] and Ding et al. [33].

The details of characteristics for regular triangle prism in each branch can be described as follows.

(a) The motion of the regular triangle prism initiates at around $U_r = 3$. Then it goes into the VIV initial branch. In this branch, the frequency ratio $f^* \ll 1$ due to the bad synchronization between the frequency of flow lift force and the frequency of oscillation and results in the low value of A^*. Additionally, as U_r increases, f^* increases rapidly due to the gradual strengthening of the synchronization, which results in the rapid increase of the value of A^* as well. These characteristics are similar to the circular cylinder, which indicates that the motion could be excited by the shedding vortices in rear wake.

(b) As the reduced velocity U_r exceeds 4.5, the motion goes into the VIV upper branch. In this range, the frequency ratio f^* jumps to a high level and approximately maintains a constant. It indicates that oscillation is in the lock-in range, and the natural frequency and the frequency of lift force are synchronized well. The amplitude ratio A^* stays at a high level and continues increasing. Nevertheless, although the performances above are similar to the circular cylinder in this range, there still exist some differences from the circular cylinder. For the triangle prism, f^* is around 0.7, which is less than the f^* of the circular cylinder. In addition, A^* still dramatically increases, and f^* stays constant; but for the circular cylinder A^* stays as a constant, and f^* increases slowly.

(c) As the reduced velocity U_r exceeds 6, the prism enters the galloping branch. In this range, the amplitude ratio A^* exceeds 1.8 and continues increasing, but the frequency ratio suddenly drops from 0.7 to 0.6 as shown in Figure 8(a). It implies that the force of shedding vortices would not be the main cause of the oscillation in the galloping branch. Contrarily, the instability of the lift force acting on the prism,

which results from the large change of the angle of attack due to the shape of the cross section, the high velocity, and the high amplitude, might be the main cause of the oscillation in this branch. It is noted that $A^*_{max} = 1.8$ is limited due to our present experimental setup. If there is no limitation, higher amplitudes could be achieved.

(d) The high damping ratio (or low system stiffness) causes the disappearance of the VIV initial branch. In our test, the damping ratio is mainly dependent on the system stiffness K, according to the expression $\zeta = c/2\sqrt{m_{osc}K}$. And the reduced velocity U_r is also dependent on the system stiffness K, according to the expressions $U_r = U/(f_n \cdot D)$ and $f_n = 1/2\pi\sqrt{K/m_{osc}}$. If m_{osc}, c, and U_r maintain their values, the flow velocity U with a high damping ratio must be lower than those with a low damping ratio. The lower flow velocity U (or Reynolds number Re) results in a lower lift force acting on the prism. This is a reasonable explanation for the disappearance of the VIV initial branch for the high damping ratio.

4.3. The Response of Right Square Prism. The right square orientation (the incident angle is 0 degrees) is one of the symmetrical configurations of the square prism. It can be observed that the performances of the right square prism are also "self-excited" but not "self-limited," which are different from the classical VIV performances of the circular cylinder (Figure 7) but are similar to the performances of the regular triangle prism (Figure 9).

As the velocity increases, the response of the amplitude has a monotonic increase trend (A^* reaches 1.2 for $U_r > 14$), the value of frequency is very low (0.4~0.7). In 1964, a linear response of amplitude for right square prism was predicted by quasi-steady theory of Den Hartog [14] and Parkinson [16]. In the present experiment, the results match well with the classical galloping response, which indicates that the main performance of the right square prism, especially at high reduced velocity, is galloping. In addition, there is a slight deviation in the amplitude trend at $U_r = 10~12$. It probably is the "kink" which was observed by Bearman in wind tunnel experiments.

It is noted that the distinction of each branch is not clear. It is still difficult to judge the initial reduced velocity of galloping even by the analysis of the variation of frequency ratio (as shown in Figures 9(b-1) and 9(b-2)). This feature is significantly different from the galloping performance of the regular triangle prism, which is probably caused by the complex vortex formation or vortex reattachment due to the cross-sectional shape.

In addition, as the damping ratio or mass ratio increases, the initial branch of vibration gradually disappears. This feature is the same as the feature of the regular triangle prism, and the reason is also the difference of lift force resulting from the change of the system stiffness.

4.4. The Response of Diamond Prism. Diamond orientation (the incident angle is 45 degrees) is another symmetrical configuration of the square prism. In Figure 10, the initial branch, the upper branch, and the lower branch or the

desynchronization can be clearly observed as the reduced velocity U_r increases for all cases. These features are comparable with those of the circular cylinder. It indicates that the diamond prism undergoes a "self-excited" and "self-limited" performance. Similar results of diamond prisms were presented by Nemes et al. [12], Zhao et al. [13], and Ding et al. [33].

The details of characteristics in each branch for the diamond prism are summarized as follows.

(a) The frequency of the lift force is low because the low flow velocity is in the initial branch. Then the bad synchronization between the lift force and oscillation causes the low value of the frequency ratio ($f^* < 1$), which results in the very low value of the amplitude ($A^* = 0.2\sim0.3$). However, as the reduced velocity U_r increases, both f^* and A^* increase rapidly due to the strengthening of the synchronization. These features are the same as the circular cylinder.

(b) When U_r increases to the upper branch, the resonant response is observed clearly. In this branch, the frequency ratio f^* is significantly close to 1, and the slope of f^* against the reduced velocity U_r presents a slight drop. That means the vibration is locked well on the shedding vortices (or lift force), and it is the reason why the amplitude jumps to and remains at a high value until the end of the branch. The features above are very close to the circular cylinder, but the following features are contrarily different from the circular cylinder. The peaks of A^* are obviously smaller (for the diamond prism, A^*_{max} = 0.4~0.5; for the circular cylinder A^*_{max} = 1~1.2), and the range of reduced velocity in the upper branch (lock-in range) is wider. It is probably because of the changes of the lift force and the vortex formation due to the sharp corners in the cross section.

(c) When the reduced velocity U_r exceeds 7, the diamond prism starts to present a drop in the responses of the amplitude as the reduced velocity moves away from the lock-in range and goes into the lower branch or the desynchronization. Meanwhile, the frequency ratio f^* increases rapidly again due to the desynchronization of the motion and the lift force, leading to the drop in amplitude. It is noted that these features above are similar to the circular cylinder; there still are two significant differences in the drop of the amplitude between the two cylinders. Firstly, the slope of the drop for the diamond prism is obviously smaller. Secondly, as m^* increases, the slope becomes too small to distinguish the upper branch, the lower branch, and the desynchronization.

(d) In addition, influences of the damping ratio and the mass ratio on the oscillation of the diamond prism are the same as the circular cylinder. A higher damping ratio leads to a higher amplitude ratio, while a lower mass ratio leads to a wider lock-in range of reduced velocity.

Therefore, we can conclude that the diamond prism undergoes a special "self-excited" and "self-limited" vibration which is different from the classical VIV of circular cylinder.

5. The Energy Transfer Ratio and the Influential Factors

In this section, the energy transfer ratios for different cylinders or prisms are calculated, analyzed, and compared. Then the impacts of the damping ratios and the mass ratios on the energy transfer ratios are investigated, respectively.

In order to ensure the reliability of the results, the energy transfer ratios were all calculated based on the experimental results. The mechanical power of oscillation P_{mech} was calculated by integration method with a time step of 0.02 s. The displacement y was measured by the magnetic induction displacement transducer; the velocity of oscillation $\dot{y}$ was the differential of the displacement; and the acceleration of $\ddot{y}$ oscillation was the differential of the velocity $\dot{y}$. The mechanical damping coefficient c was calculated by the tested results of damping ratios ζ presented in Table 3. In addition, the flow energy power P_w was calculated by (9a). The flow velocity U was measured by the Pitot tube. Finally η was calculated by $\eta = P_{mech}/P_w$.

5.1. The Performances of the Transfer Ratio For Different Oscillators. The variations of the energy transfer ratios with the reduced velocity for different cylinders or prisms are plotted in Figure 11. Then the following characteristics are obtained.

It is observed that the variations of the transfer ratios for the circular cylinder and the right square prism are similar. Prior to a critical reduced velocity, the transfer ratio increases until a maximum value is reached. Then the ratio slowly diminishes to a low value. It can be found that that the critical reduced velocity ($U_r \approx 5$) is actually the boundary to distinguish the VIV initial and the upper branch. These features can be attributed to the "self-excited" and the "self-limited" motion for the two cylinders (or prisms). After reaching the critical reduced velocity ($U_r \approx 5$), the oscillation enters the lock-in range (VIV upper branch). In this range, the amplitude and frequency approximately maintain a constant or increase very slowly. This results in a slow increase of the mechanical power. By contrast, the flow energy power grows very fast due to the increasing flow velocity. Therefore, the transfer ratios collapse after the critical velocity.

The variations of the transfer ratios for the regular triangle and right square prism are different from those of the circular cylinder and diamond prism. For the triangle prism, the transfer ratio asymptotically maintains a constant after reaching the critical reduced velocity, which differs from the circular cylinder. For the right square prism, the transfer ratio continuously increases without any sign of decrease. These features can all be attributed to the "self-excited" and the "self-unlimited" motion (galloping) with a monotonic increase in amplitude.

In addition, the transfer ratios of the diamond and right square prism, which are 6% and 1.8%, are much lower than those of the circular cylinder and the triangle prism, which are 80% and 57%. The reasons can be found from the responses in Figures 9 and 10. For the right square prism, the

initiation of oscillation needs a higher flow velocity resulting in a higher value of flow power P_w. For the diamond prism, the values of amplitude ratios and frequency ratios are much lower than those of other prisms.

The features above demonstrate that the capacities of energy transference for the square prisms are lower than those of circular cylinders and triangle prisms to some degrees. Therefore, it is more reasonable to use a circular cylinder or triangle cylinder in the design of the energy conversion from the FIM.

5.2. The Influential Factors. The roles of mass and damping are investigated in this section. In the majority of previous studies, mass and damping are regarded as a combined parameter to affect the performance of FIM. In this study, the influences of mass and damping are analyzed independently.

Before the analysis of the influence of the damping ratio, the combined parameter $(A^* f^*)^2/U_r^3$ is introduced first. It could be concluded from the expression of the energy transfer ratio (see (14a)) that if other factors are fixed, the transfer ratio would increase linearly with the combined parameter. Figure 12 plots the relationships between the transfer ratio and the combined parameter for three different damping ratios. Meanwhile, four configurations are compared in this figure, which are the circular cylinder with mass ratio $m^* = 4.2$, the circular cylinder with mass ratio $m^* = 2.2$, the regular triangle prism with mass ratio $m^* = 4.2$, and the diamond prism with mass ratio $m^* = 4.2$. As expected, the transfer ratio shows an approximate linear trend with the combined parameter $(A^* f^*)^2/U_r^3$. It soundly proves the conclusion above deduced from the expression of the transfer ratio (see (14a)).

According to Figure 12, the transfer ratios, including the maximum transfer ratios, are strongly dependent on the damping ratios for all configurations. The lower the damping ratio is, the lower the transfer ratio is. This feature also agrees well with the expression of the transfer ratio. It is noted that the increase of the damping ratio is actually caused by the decrease of the system stiffness in the present experiments. In conclusion, the increase of the damping ratio or the decrease of the system stiffness can cause a high mechanical energy of FIM leading to a high capacity of the energy transference.

In order to investigate the influences of the mass ratio, two cases with similar damping ratios but different mass ratios are illustrated in Figure 13. It is hard to maintain the damping ratios at the same value for different mass ratios because of the limitation of the experiment setup. So we compared two configurations with similar damping ratios in all cases.

It is concluded from the discussion of the influences of the damping ratio that a higher damping ratio would cause a higher transfer ratio when the mass ratios are the same. Then the transfer ratio at $\zeta = 0.1036$ and $m^* = 4.2$ would be higher than that at $\zeta = 0.0884$ and $m^* = 4.2$. In Figure 13(a), it is clearly observed that the maximum of the transfer ratio at $\zeta = 0.0884$ and $m^* = 4.2$ is higher than that at $\zeta = 0.1036$ and $m^* = 2.2$. Then we could conclude that the maximum of transfer ratio at $\zeta = 0.1036$ and $m^* = 4.2$ would be higher than that at $\zeta = 0.1036$ and $m^* = 2.2$. A similar

conclusion could also be drawn from the Figure 13(b). These results indicate that the maximum of the transfer ratio is strongly dependent on the mass ratio. The higher the mass ratio is, the higher the transfer ratio is. The characteristics of mass ratio can also correlate with the expression of transfer ratio. In conclusion, the increase of the mass ratio will also strengthen the capacity of energy transference from the flow.

In addition, the reduced velocity corresponding to the maximum transfer ratio is dependent on the mass ratio. This result agrees well with the result in Barrero-Gil et al.'s studies [29].

6. The Stationarity of Oscillation

6.1. The Evaluation of the Stationarity of the Amplitude. Four typical examples of the time histories of displacement in each branch, for the cylinders with different cross sections, are illustrated in Figure 14. It could be found that the circular cylinder experienced a quasiperiodic oscillation in the upper branch ($U_r = 5.03$), which means each amplitude in this branch approximately maintains a constant. Similar behaviors can also be observed in the upper branch ($U_r = 4.86$) and galloping branch ($U_r = 7.48$) for the regular triangle prism and in the upper branch ($U_r = 5.02$) for the diamond prism. This feature is mainly attributed to the great synchronization of the oscillation and the lift force. By contrast, the amplitudes in other cases could not maintain a constant in each period due to the bad synchronization of the oscillation and the lift force. Hence, the different configurations (cross sections, velocities, etc.) result in different amplitudes in the time histories of displacement.

As we know, the electrical power quality is strongly dependent on the steady output of the convertor. For the energy extracted from the FIM, the steady output is strongly dependent on the steady mechanical power of the oscillator, and the steady mechanical power is strongly dependent on the steady performances of the amplitudes. Consequently, it is necessary to obtain the stationarity of the amplitude to estimate the quality of the mechanical power.

The variation coefficient of amplitude, CV, is introduced to estimate the stationarity of the amplitude, which is expressed as

$$\mathrm{CV} = \frac{\sigma}{\overline{A}} = \frac{\sqrt{(1/N)\sum_{i=1}^{N}\left(A_i - \overline{A}\right)^2}}{\overline{A}}, \tag{18}$$

where σ denotes the standard deviation of the amplitudes, $\overline{A}$ is the average of the amplitudes, N is the number of the amplitudes, and A_i is the ith amplitude.

According to the definition and the expression of CV, we can conclude that a low value of CV would achieve a good stationarity of the amplitude.

6.2. The Relationship between the Stationarity and the Energy Transfer Ratio. In this section, the relationships between the stationarity of the amplitude and the capacity of energy transference are discussed. CV values were calculated based on the experimental results, and A_i values were extracted

from the time histories of the displacements. Then variations of CV against the transfer ratio η were plotted in Figure 15 for each cylinder.

As seen in Figure 15, similar variations of CV are observed for different cylinders. As η increases, CV collapses down rapidly from a high value for all cases. After a critical transfer ratio, CV diminishes slowly asymptotically to a constant value. Therefore, if the transfer ratio is controlled to be over the critical transfer ratio, the quality of the mechanical energy of the oscillators will be remarkably improved.

For the circular cylinder, the critical transfer ratio and the constant value of CV are 40% and 20%. For the regular triangle prism, the two parameters are 17% and 10%. For the right square prism, they are 1.5% and 30%. For the diamond prism, they are 7% and 30%. Obviously, the regular triangle prism and the circular cylinder present a better performance of the stationarity.

7. Conclusion

This paper focuses on the characteristics of FIM and the capacity of energy transference from the flow for cylinders or prisms with different cross sections. According to the motion of the cylinder, the energy transfer ratio of mechanical energy and the flow power was derived, and the influential factors were pointed out. Then an experimental setup was designed and verified. Experiments using spring-mounted rigid cylinders with different configurations, which include cross section, mass ratio, and damping ratio, were performed. The characteristics of flow induced motion with different configurations were investigated and compared with each other. The mechanical power and energy transfer ratio were calculated based on the experimental results. The performances of transfer ratio with different cross sections were compared. The impacts of influential factors were analyzed. Finally, the oscillating stationarity was discussed, and an evaluating index was proposed. The relationship between the energy transfer ratio and the stationarity was analyzed. The following conclusions can be drawn.

(a) Circular cylinders and diamond prisms both present "self-excited" and "self-limited" motions. Three VIV branches can be clearly observed in the responses. However, there are still a few differences between these two cylinders. The peak of amplitude ratio A^* for circular cylinder, which is around 1~1.2, is significantly larger than that of diamond prism (0.4~0.5). The lock-in range of diamond prism, which is from $U_r = 4$ to $U_r = 7$, is wider than the circular cylinder. Also the slopes of drop in the amplitude for diamond prisms are slower than that for circular cylinders when the cylinders enter the lower branch or desynchronization range.

(b) Triangle prisms and right square prisms present "self-excited" but "self-unlimited" motions. For triangle prism, when U_r exceeds 7, A^* increases over 1.8, but f^* collapses to 0.6. For right square prisms, when U_r exceeds 14, A^* reaches 1.2, and f^* decreases to around 0.4~0.7. Three branches, which are the VIV initial branch, VIV upper branch, and fully developed galloping branch, can be clearly observed in the responses of triangle prisms. For right square prisms, it

is hard to distinguish each branch in the response due to the complicated vortex structures.

(c) The maximum transfer ratios of circular cylinders and triangle prisms, which are 80% and 57%, are dramatically larger than those of right square prisms and diamond prisms due to the higher amplitudes or the higher frequencies, indicating that the circular cylinder and triangle prism have a better capacity in energy transference. The circular cylinder does a good job in an appropriate velocity range due to the "self-limited" feature. By contrast, the triangle prism performs well in the velocity range with no limitation due to the "self-unlimited" feature.

(d) The energy transfer ratio is strongly dependent on the damping ratio and mass ratio. The higher damping ratio promotes higher transfer ratio. The higher mass ratio promotes the higher peak of the transfer ratio and the corresponding reduced velocity.

(e) The variation coefficient of amplitude CV is introduced to estimate the stationarity of the oscillation. The transfer ratio should be maintained over the critical value to achieve a better performance in the stationarity. Beyond the critical transfer ratios, variation coefficient of amplitude CV is around 10%~30%. The circular cylinder and the triangle prism perform better than the square prisms in stationarity.

Competing Interests

The authors declare no conflict of interests.

Acknowledgments

References

[1] M. T. Song, D. Q. Cao, and W. D. Zhu, "Vortex-induced vibration of a cable-stayed bridge," *Shock and Vibration*, vol. 2016, Article ID 1928086, 14 pages, 2016.

[2] A. D. Trim, H. Braaten, H. Lie, and M. A. Tognarelli, "Experimental investigation of vortex-induced vibration of long marine risers," *Journal of Fluids and Structures*, vol. 21, no. 3, pp. 335–361, 2005.

[3] R. D. Blevins, *Flow-Induced Vibration*, Van Nostrand Reinhold, New York, NY, USA, 3th edition, 1990.

[4] C. C. Feng, *The Measurement of Vortex Induced Effects in Flow Past Stationary and Oscillating Circular and D-Section Cylinders*, Diss. University of British Columbia, 1968.

[5] P. W. Bearman, "Vortex shedding from oscillating bluff bodies," *Annual Review of Fluid Mechanics*, vol. 16, no. 1, pp. 195–222, 1984.

[6] T. Sarpkaya, "A critical review of the intrinsic nature of vortex-induced vibrations," *Journal of Fluids and Structures*, vol. 19, no. 4, pp. 389–447, 2004.

[7] C. H. Williamson and R. Govardhan, "Vortex-induced vibrations," in *Annual Review of Fluid Mechanics*, vol. 36 of *Annu. Rev. Fluid Mech.*, pp. 413–455, Annual Reviews, Palo Alto, Calif, USA, 2004.

[8] A. Khalak and C. H. K. Williamson, "Fluid forces and dynamics of a hydroelastic structure with very low mass and damping," *Journal of Fluids and Structures*, vol. 11, no. 8, pp. 973–982, 1997.

[9] A. Khalak and C. H. K. Williamson, "Motions, forces and mode transitions in vortex-induced vibrations at low mass-damping," *Journal of Fluids and Structures*, vol. 13, no. 7-8, pp. 813–851, 1999.

[10] R. Govardhan and C. H. Williamson, "Modes of vortex formation and frequency response of a freely vibrating cylinder," *Journal of Fluid Mechanics*, vol. 420, pp. 85–130, 2000.

[11] K. Raghavan and M. M. Bernitsas, "Experimental investigation of Reynolds number effect on vortex induced vibration of rigid circular cylinder on elastic supports," *Ocean Engineering*, vol. 38, no. 5-6, pp. 719–731, 2011.

[12] A. Nemes, J. Zhao, D. Lo Jacono, and J. Sheridan, "The interaction between flow-induced vibration mechanisms of a square cylinder with varying angles of attack," *Journal of Fluid Mechanics*, vol. 710, pp. 102–130, 2012.

[13] J. Zhao, J. S. Leontini, D. Lo Jacono, and J. Sheridan, "Fluid-structure interaction of a square cylinder at different angles of attack," *Journal of Fluid Mechanics*, vol. 747, no. 2, pp. 688–721, 2014.

[14] J. P. Den Hartog, *Mechanical Vibrations*, McGraw-Hill, New York, NY, USA, 4th edition, 1956.

[15] G. Alonso and J. Meseguer, "A parametric study of the galloping stability of two-dimensional triangular cross-section bodies," *Journal of Wind Engineering and Industrial Aerodynamics*, vol. 94, no. 4, pp. 241–253, 2006.

[16] G. Parkinson, "Phenomena and modelling of flow-induced vibrations of bluff bodies," *Progress in Aerospace Sciences*, vol. 26, no. 2, pp. 169–224, 1989.

[17] T. Tamura and Y. Itoh, "Unstable aerodynamic phenomena of a rectangular cylinder with critical section," *Journal of Wind Engineering and Industrial Aerodynamics*, vol. 83, no. 1, pp. 121–133, 1999.

[18] A. Barrero-Gil and P. Fernandez-Arroyo, "Maximum Vortex-Induced Vibrations of a square prism," *Wind and Structures*, vol. 16, no. 4, pp. 341–354, 2013.

[19] G. Alonso, J. Meseguer, and I. Pérez-Grande, "Galloping instabilities of two-dimensional triangular cross-section bodies," *Experiments in Fluids*, vol. 38, no. 6, pp. 789–795, 2005.

[20] G. Alonso, J. Meseguer, and I. Pérez-Grande, "Galloping stability of triangular cross-sectional bodies: a systematic approach," *Journal of Wind Engineering and Industrial Aerodynamics*, vol. 95, no. 9-11, pp. 928–940, 2007.

[21] P. Muralt, "Ferroelectric thin films for micro-sensors and actuators: a review," *Journal of Micromechanics and Microengineering*, vol. 10, no. 2, pp. 136–146, 2000.

[22] K. Guo, S. Cao, and S. Wang, "Numerical and experimental studies on nonlinear dynamics and performance of a bistable piezoelectric cantilever generator," *Shock and Vibration*, vol. 2015, Article ID 692731, 14 pages, 2015.

[23] A. Mehmood, A. Abdelkefi, M. R. Hajj, A. H. Nayfeh, I. Akhtar, and A. O. Nuhait, "Piezoelectric energy harvesting from vortex-induced vibrations of circular cylinder," *Journal of Sound and Vibration*, vol. 332, no. 19, pp. 4656–4667, 2013.

[24] M. M. Bernitsas, K. Raghavan, Y. Ben-Simon, and E. M. H. Garcia, "VIVACE (vortex induced vibration aquatic clean energy): a new concept in generation of clean and renewable energy from fluid flow," *Journal of Offshore Mechanics and Arctic Engineering*, vol. 130, no. 4, Article ID 041101, 15 pages, 2008.

[25] M. M. Bernitsas, Y. Ben-Simon, K. Raghavan, and E. M. H. Garcia, "The VIVACE converter: model tests at high damping and reynolds number around 10^5," *Journal of Offshore Mechanics and Arctic Engineering*, vol. 131, no. 1, pp. 1–12, 2009.

[26] H. Park, R. A. Kumar, and M. M. Bernitsas, "Enhancement of flow-induced motion of rigid circular cylinder on springs by localized surface roughness at 3×104≤Re≤1. 2×105," *Ocean Engineering*, vol. 72, pp. 403–415, 2013.

[27] J. H. Lee, N. Xiros, and M. M. Bernitsas, "Virtual damper-spring system for VIV experiments and hydrokinetic energy conversion," *Ocean Engineering*, vol. 38, no. 5-6, pp. 732–747, 2011.

[28] H. Sun, E. S. Kim, M. P. Bernitsas, and M. M. Bernitsas, "Virtual spring-damping system for flow-induced motion experiments," *Journal of Offshore Mechanics and Arctic Engineering*, vol. 137, no. 6, Article ID 061801, 2015.

[29] A. Barrero-Gil, G. Alonso, and A. Sanz-Andres, "Energy harvesting from transverse galloping," *Journal of Sound and Vibration*, vol. 329, no. 14, pp. 2873–2883, 2010.

[30] A. Barrero-Gil, S. Pindado, and S. Avila, "Extracting energy from Vortex-Induced Vibrations: a parametric study," *Applied Mathematical Modelling*, vol. 36, no. 7, pp. 3153–3160, 2012.

[31] H. L. Dai, A. Abdelkefi, and L. Wang, "Theoretical modeling and nonlinear analysis of piezoelectric energy harvesting from vortex-induced vibrations," *Journal of Intelligent Material Systems and Structures*, vol. 25, no. 14, pp. 1861–1874, 2014.

[32] H. L. Dai, A. Abdelkefi, and L. Wang, "Piezoelectric energy harvesting from concurrent vortex-induced vibrations and base excitations," *Nonlinear Dynamics*, vol. 77, no. 3, pp. 967–981, 2014.

[33] L. Ding, L. Zhang, C. Wu, X. Mao, and D. Jiang, "Flow induced motion and energy harvesting of bluff bodies with different cross sections," *Energy Conversion and Management*, vol. 91, pp. 416–426, 2015.

[34] G. V. Iungo and G. Buresti, "Experimental investigation on the aerodynamic loads and wake flow features of low aspect-ratio triangular prisms at different wind directions," *Journal of Fluids and Structures*, vol. 25, no. 7, pp. 1119–1135, 2009.

[35] Y. Nishi, "Power extraction from vortex-induced vibration of dual mass system," *Journal of Sound and Vibration*, vol. 332, no. 1, pp. 199–212, 2013.

[36] Y. Nishi, Y. Ueno, M. Nishio, L. A. R. Quadrante, and K. Kokubun, "Power extraction using flow-induced vibration of a circular cylinder placed near another fixed cylinder," *Journal of Sound and Vibration*, vol. 333, no. 10, pp. 2863–2880, 2014.

[37] M. A. Dhanwani, A. Sarkar, and B. S. V. Patnaik, "Lumped parameter models of vortex induced vibration with application to the design of aquatic energy harvester," *Journal of Fluids and Structures*, vol. 43, pp. 302–324, 2013.

[38] J. Zhang, G. Xu, F. Liu, J. Lian, and X. Yan, "Experimental investigation on the flow induced vibration of an equilateral triangle prism in water," *Applied Ocean Research*, vol. 61, pp. 92–100, 2016.

[39] S. Szepessy and P. W. Bearman, "Aspect ratio and end plate effects on vortex shedding from a circular cylinder," *Journal of Fluid Mechanics*, vol. 234, pp. 191–217, 1992.

[40] S. Szepessy, "On the control of circular cylinder flow by end plates," *European Journal of Mechanics B: Fluids*, vol. 12, pp. 217–244, 1993.

[41] T. L. Morse, R. N. Govardhan, and C. H. K. Williamson, "The effect of end conditions on the vortex-induced vibration of

cylinders," *Journal of Fluids and Structures*, vol. 24, no. 8, pp. 1227–1239, 2008.

[42] J. Zhang, *Experimental Investigation on the Flow Induced Vibration and Energy Extraction of an Equilateral Triangle Prism*, Tianjin University, 2016 (Chinese).